Geochemistry, Geophysics, Geosystems

RESEARCH ARTICLE
10.1029/2020GC009136

Quantification of Eruption Dynamics on the North Rift at Axial Seamount, Juan de Fuca Ridge

M. Le Saout[1,2], D. R. Bohnenstiehl[3], J. B. Paduan[1], and D. A. Clague[1]

[1]Monterey Bay Aquarium Research Institute, Moss Landing, CA, USA, [2]Now at Department of Magmatic and Hydrothermal Systems, GEOMAR Helmholtz Centre for Ocean Research, Kiel, Germany, [3]Department of Marine, Earth and Atmospheric Sciences and Center for Geospatial Analytics, North Carolina State University, Raleigh, NC, USA

Key Points:
- AUV mapping along the north rift identifies hummocky mounds with pillows, channelized, and inflated flows formed during the 2015 eruption
- Impulsive sounds formed by lava/seawater interaction track mound growth over a 28-day period with an average extrusion rate of 22–45 $m^3\ s^{-1}$
- The sounds record the history of flow advancement and inflation from multiple eruptive centers and are used to infer volcanic activity style

Supporting Information:
- Supporting Information S1

Correspondence to:
M. Le Saout,
mlesaout@geomar.de

Citation:
Le Saout, M., Bohnenstiehl, D. R., Paduan, J. B., & Clague, D. A. (2020). Quantification of eruption dynamics on the north rift at Axial Seamount, Juan de Fuca Ridge. *Geochemistry, Geophysics, Geosystems*, *21*, e2020GC009136. https://doi.org/10.1029/2020GC009136

Received 27 APR 2020
Accepted 27 JUL 2020
Accepted article online 2 AUG 2020

Abstract Quantifying eruption dynamics in submarine environments is challenging. During the 2015 eruption of Axial Seamount, the formation of hummocky mounds along the north rift was accompanied by tens of thousands of impulsive acoustic signals generated by the interaction of lava and seawater. A catalog of these sounds was integrated with detailed seafloor mapping to better understand eruptive processes in time and space. Mounds grew over a period of 28 days with average extrusion rates of 22 to 45 $m^3\ s^{-1}$. The most distant mounds, ~9.5 to 15.5 km down rift from the caldera, grew primarily over the first few days of the eruption. The focus of eruptive activity then retreated ~5 km toward the caldera where it was sustained. Mounds are constructed as a series of superimposed lobes formed through alternating periods of flow inflation, generating up to 30-m-thick hummocks, and periods of flow advancement, with $<0.02\ m\ s^{-1}$ average speeds typically observed.

Plain Language Summary In 2015, a deep sea volcanic eruption occurred at Axial Seamount. It is challenging to determine parameters such as eruption timing, volume of lava erupted on the seafloor, or speed of emplacement without direct observations. To study these eruption processes, we used 1-m resolution bathymetric maps acquired after the eruption, which provided information on the volume and shape of the lava flows, and hydroacoustic data that tracked the sounds generated as hot lava interacted with cold seawater. We found that on the north rift of Axial Seamount, the eruption lasted 28 days. It was not continuous but had periods of emplacement of new lava flows and periods of inflation of those preexisting flows into mounds of lava up to 30 m high. These variations in eruption style produce the complex flow morphology observed at Axial Seamount.

1. Introduction

Despite mid-ocean ridges being the most extensive volcanic system on Earth, the lack of direct eruption observations limits our knowledge about the dynamics of those eruptions. Lava flow morphologies have commonly been used as a proxy for eruptive processes (Gregg & Fink, 1995; Griffiths & Fink, 1992; Meyer & White, 2007). However, eruptions are complex and produce flows not limited to a uniform morphology. Different approaches have been used to get a better constraint on the eruption dynamic, like numerical modeling of diffusion-controlled bubble growth or the measurements of dissolved volatiles and distribution and size of vesicle within the basalt (Jones et al., 2018; Soule et al., 2012). Monitoring of active submarine volcanoes with repeated autonomous underwater vehicle (AUV) surveys and in situ geophysical sensors can also provide better constraints on eruption timing and effusion rates, which influence flow dimensions and morphology (e.g., Clague et al., 2017; Dziak & Fox, 1999; Nooner & Chadwick, 2016; Soule et al., 2007; Tolstoy et al., 2006).

Axial Seamount erupted in 1998, 2011, and 2015 (Caress et al., 2012; Chadwick et al., 2013, 2016). The latest eruption was monitored in situ by seismic stations, hydrophones, tiltmeters, and pressure sensors deployed near the volcano's summit as part of the OOI Cabled Array (Figure 1; Kelley et al., 2014). These geophysical records have enabled the determination of the eruption timing, and repeated AUV surveys have defined eruptive volumes and flow morphologies (e.g., Clague et al., 2017; Wilcock et al., 2016). On 24 April 2015, an increase in seismicity began at ~04:20 UTC (Wilcock et al., 2016), followed by rapid deflation and tilting of the caldera floor at ~06:00 UTC when the volcanic eruption began (Nooner & Chadwick, 2016). Lava began to flow on the eastern side of the caldera and the dike rapidly propagated to the north rift at a speed of $0.7\ m\ s^{-1}$ over a distance of 20 km (Chadwick et al., 2016; Wilcock et al., 2016, 2018). The total area of $11.5 \times 10^6\ m^2$ and volume of $155.2 \times 10^6\ m^3$ of lava erupted on the seafloor was calculated from the

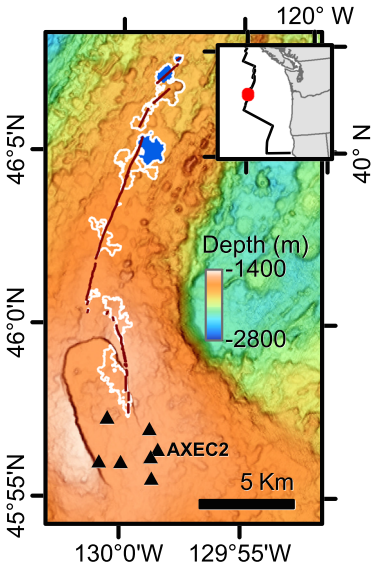

Figure 1. Bathymetric map of the caldera and north rift of Axial Seamount. The 2015 lava flows are outlined in white and eruptive fissures in brown. The three hummocky flows studied in this paper are colored in blue. Black triangles indicate stations in the cabled array of the Ocean Observatories Initiatives (OOI). Inset locates Axial Seamount (in red) off the west coast of the United States on the boundary between the Pacific and Juan de Fuca tectonic plates (black line).

difference between pre-eruption and post-eruption bathymetry (Chadwick et al., 2016; Clague et al., 2017), although only the flows within and near the summit were located where pre-eruption high-resolution AUV surveys had been completed.

Impulsive hydroacoustic signals recorded by hydrophones on the caldera floor, thought to be caused by lava-water interactions, were sourced from flows within the caldera and along the north rift (Caplan-Auerbach et al., 2017; Wilcock et al., 2016; Figure S1 in the supporting information). They began at about 08:00 UTC, soon after onset of the seismic crisis, on 24 April and continued until 21 May, when lava extrusion is inferred to have ended, and the subsidence of the caldera floor stopped (Wilcock et al., 2016). Waveform similarity extending to high frequencies (50–100 Hz) indicates a repetitive source process with groups of up to 25 multiplets originating from source areas that are only a few meters in diameter (Caplan-Auerbach et al., 2017). Chadwick et al. (2016) and Clague et al. (2017) attributed the sounds in and near the caldera to small steam explosions occurring when rapidly advancing channelized flows entrapped seawater underneath, which heated and expanded to steam. These small explosions create craters of meter to several meter scale surrounded by shattered lava fragments. These are most commonly observed within several meters of flow margins but occur throughout the flow. Similar acoustic signals recorded along the East-Pacific Rise at 9°50′N (Tan et al., 2016) and on the Gakkel ridge (Schlindwein et al., 2005; Schlindwein & Riedel, 2010) suggest that these types of impulsive sounds may be common during mid-ocean ridge eruptions independently of the spreading rate. Acoustic recordings during the 2015 Axial eruption also include a series of diffuse broadband sounds lasting from ~2 min to an hour. Caplan-Auerbach et al. (2017) attribute this signal to Hawaiian-style fountains that produced pyroclastic ash recovered near the center of the caldera (Chadwick et al., 2016; Clague et al., 2018).

In this study, we present a detailed analysis of the emplacement of three edifices on the north rift of Axial Seamount during the 2015 eruption (Figure 1). The edifices selected have well defined boundaries and show variation in dimension, morphology of their summit, and duration of the impulsive sound. Combining the spatial and temporal distribution of impulsive signals with 1-m resolution bathymetry, we investigate small variations in the flow front velocity and determine the location of multiple extrusion sources within a single flow in order to analyze the dynamics of the eruption.

2. Data and Methods

2.1. Data

This study is primarily based on two set of data: AUV-bathymetry and the seismo-acoustic data. AUV bathymetric data were collected during multiple AUV surveys, before and after the 2015 eruption. All the new lava flows formed during the 2015 eruption were mapped with the Woods Hole Oceanographic Institution (WHOI) AUV *Sentry* and MBARI Mapping AUVs (Chadwick et al., 2016; Clague et al., 2017), which produce data with 1-m lateral resolution. Acoustic and seismic data were collected by the OOI network (Figure 1). The OOI network consists of seven ocean bottom stations along the caldera floor and rim. Two (AXCC1 and AXEC2) are instrumented with three-component broadband seismometers and low-frequency acoustic receivers (hydrophones), and five have short-period three-component seismometers. All seismic and acoustic data are sampled at a rate of 200 Hz. The data were analyzed for earthquake and impulsive signals (Caplan-Auerbach et al., 2017; Mann et al., 2016; Wilcock et al., 2016; Figure S1).

2.2. Hydroacoustic Processing

In the catalog used here, high-frequency (50–100 Hz) impulsive acoustic events were identified on station AXEC2 by matching waveforms against a suite of 817 waveform templates chosen from isolated arrivals, with high signal to noise, that span the eruptive period. Template matching using three-component

(HDH, HHZ, and HHN) waveforms returned a set of >37,000 detections (correlation coefficient >0.7). For each detection on AXEC2, the vertical (HHZ) channel waveform was cross correlated against the other six OOI stations within the caldera to precisely determine the time of the first (sea surface reflected) and second (sea surface and seafloor reflected) arriving phases across the network. Locations were determined using a grid search with a 25 × 25 m spatial resolution. Travel times for both phases were computed, assuming a planar sloping seafloor between the source and each receiver with a constant sound velocity of 1,485 m s^{-1}. The final catalog contains locations for ~22,000 impulsive sounds constrained using at least seven arriving phases, with an average root mean square error of 0.022 s. The mean location uncertainty is ~140 m (χ^2 − misfit at 68% confidence); however, there are additional range-dependent location biases related to anomalies in the water column velocity structure and unmodeled bathymetric effects, which influence the travel times of the sea surface and seafloor bouncing arrivals recorded in the caldera. These biases are quantified by manually aligning the contoured impulsive sound density maps with the flow boundaries, as documented in Figure S2. All data presented consider the signal locations after bias correction. Potential misalignment of the acoustic events does not impact the determination of flow front velocity, as this bias is quantified for individual mounds and not individual events. The peak amplitude of each arrival was measured and corrected for geometric spreading loss to estimate the source level (units of dB re 1 μPa at 1 m).

The diffuse, longer duration, broadband signals recorded from 1 May until 20 May were small in amplitude and their arrivals emergent in character, so not easily located (Caplan-Auerbach et al., 2017). Therefore, no catalog of these signals was produced, and only the time frame of their activity is used in our interpretation.

2.3. Lava Flow Delineation and Volume Determination

Lava flows emplaced during the 2015 eruption were delineated using the difference between maps of pre-eruption and post-eruption bathymetry. At the summit of Axial Seamount, AUV mapping at 1-m lateral resolution before (Clague et al., 2013) and after (Chadwick et al., 2016) allowed precise flow boundary determination and volume calculation of the thin new flows within the caldera and on the upper north rift (Chadwick et al., 2016). The distal north rift zone of the volcano had not been mapped with AUVs prior to the eruption, so ship-collected multibeam bathymetry (Chadwick et al., 2016) served as the pre-eruption map to compare with the MBARI AUV-bathymetry collected post-eruption for the 2015 flows deeper than ~1,600 m (Clague et al., 2017). Flow volumes, therefore, are not as well defined for the distal flows, although the greater flow thickness minimizes errors in volume estimates. Lava flow boundary identification and area calculations improved following examination of the 1-m resolution bathymetry and observations on dives J2-826 of the WHOI ROV *Jason* and D879 of the MBARI ROV *Doc Ricketts* (Chadwick et al., 2016; Clague et al., 2017). The AUV bathymetry, supported by ROV dive observations, is used to analyze flow texture and delimit individual lobes, channels, and collapses, and tumuli within the flows.

2.4. Estimation of Flow Front Velocity

The morphology and distribution of acoustic events were analyzed for three mounds between 46°4.5′N and 46°7.8′N. Other edifices were built during the 2015 eruption; however, they formed coalesced structures with poorly defined boundaries between mounds, especially for the acoustic events. The analyses of the distribution of the acoustic events were primarily done using the ArcGIS point profile interactive tool. When looking at the mound scale, acoustic events were selected for an entire mound projected on a line perpendicular to the eruptive fissure. For individual clusters, the acoustic data were projected in multiple directions. Flow front velocity was determined along those profiles between the first acoustic event at the beginning of the cluster and the first acoustic event at the end of the cluster (Figure S3). The axis showing the fastest flow front velocity is considered to represent the lava flow axis (Figure S3). When no flow front velocity was determined, the acoustic data are plot along the axis of the lobe below.

To constrain the uncertainty in flow front velocity due to the uncertainty in the location of the acoustic events, a series of simulations were conducted for each flow. The location of each acoustic event was shifted by a random Gaussian error, with a standard deviation of 140 m, and a new estimate of the flow front velocity was calculated using the simulated locations. This procedure was repeated 1,000 times for each flow, and the standard deviation of these estimates was taken to represent the uncertainty (68% confidence) in the estimated front velocity.

3. Results

During the 2015 eruption, the thickest flows were emplaced on the north rift of Axial Seamount between 46°4.5′N and 46°7.8′N, and the three discussed here are referred to as edifices H1, H2, and H3 for Hummocky Mounds 1, 2, and 3 (Figures 1 and 2). The three edifices are inflated hummocky flows (Clague et al., 2017), which mainly consist of pillow lava as indicated by the mapped flow texture and confirmed by ROV dive observations (Chadwick et al., 2016; Clague et al., 2017). Although their flow type is similar, the three mounds have different geometries and lava structures on their summits.

Edifice H1 is a complex feature 1.5 km wide, 1.7 km long, and 60 m high (Figure 2a). The bathymetric difference map indicates a volume of 51×10^6 m^3, about a third of the total volume of lava erupted in 2015 (Clague et al., 2017). The edifice consists of an intricate network of lobes, at least fifteen lobes, up to 500 m wide and 1,100 m long (Figures 2a and 2b; Clague et al., 2017). The lobes are distributed around four centers of extrusion located 230 to 820 m from the eruptive fissure (Figure 2a). Each center of extrusion corresponds to a tumulus, while collapses and inflated sheet flows characterize the axis of each lobe (Figures 2a and 2b). Margins and ends of hummocky lobes consist of pillow lava.

Edifices H2 and H3 formed above the eruptive fissures (Clague et al., 2017). Edifice H2 is a broad, flat-topped cone ringed by pillow lavas. It is 1 km in diameter and 68 m high for a volume of 22.8×10^6 m^3 (Figure 2c). No lobes are distinguishable, but its summit consists of a lava pond that overflowed to form levees and then partly drained to form shallow depressions (Clague et al., 2017). Edifice H3 is a hummocky mound 460 m in diameter and 73 m high for a volume of 5×10^6 m^3 (Figure 2c). No lobes or sheet flows are observed, but there is a tumulus 46 m long, 15 m wide, and 2 m high with a collapse pit 35 m wide and 10 m deep slightly NE of the summit center (Figure 2d).

Edifice H1 was the locus of more than 7,100 impulsive sounds over 28 days (Figure 2e). Edifice H2 experienced at least 1,240 impulsive sounds in 6 days (Figure 2f) and Edifice H3, 50 in 46 hr (Figure 2g). Impulsive sounds are used as a proxy for the duration of the eruptive activity, giving average lava extrusion rates of 22, 45, and 30 m^3 s^{-1} for Edifices H1, H2, and H3, respectively.

The acoustic signals migrated to the north at a speed of 0.3 m s^{-1} between 46°4.8′N (H1) and 46°7.8′N (H3), tracking the onset of eruptive activity fed by the dike propagating along the north rift (Figure 3a). The northern lava flows, including Edifices H2 and H3, were constructed during the first few days of activity. Approximately 40 hr after the onset of the eruption, the focus of activity began to regress toward H1, as the average source level of these sounds also decreased (Figure 3a). During the next 4 days, activity became increasingly localized near H1, where it was sustained as the construction of the mound continued over the next 3 weeks.

The progression of acoustic events at each hummock with distance from the eruptive fissure is shown in Figures 3b–3d. At Edifice H1, the acoustic signal was discontinuous and distributed in dense clusters, or bursts (Figure 3b). The first burst occurred only 8 hr after the beginning of the eruption in the caldera (Figure 4 and Table 1). The sounds propagated from the eruptive fissure over a distance of 629 m. The flow front velocity estimated on a straight line perpendicular to the fissure reached 0.039 m s^{-1} with the density of impulsive sounds higher at the flow front (Figure 4a). Successive bursts of impulsive sounds initiated from four different extrusion centers located 250 to 800 m from the eruptive fissure and were often associated with the highest impulsive sound densities (Figures 3b and 4). Those extrusion centers coincide with tumuli identified from the AUV bathymetry (Figure 2a). Only major off-axis extrusion centers have been identified. They consist in large tumuli probably located at the vertical of major lava tubes and mark the point of origin of several lava flow.

Eight periods of the eruption with bursts of impulsive sounds are shown in Figure 4. Individual bursts occurred over distances of 170 to 629 m during periods of a few to a hundred hours (Table 1). Some acoustic bursts had a time-distance correlation that allows the determination of the advancement rate, while others occurred at the same time along the lobe (Figures 4 and S4). Estimated flow-front advancement rates range from 0.004 to 0.038 m s^{-1} (Table 1). Each burst of impulsive sounds can be associated with the growth of one or two lobes around a single extrusion center. The lobes emplaced at the same time are characterized by similar flow front velocity (Figure 4 and Table 1). However, there is no evidence that two or more bursts of impulsive sounds started at the same time from different extrusion centers, but acoustic signals often

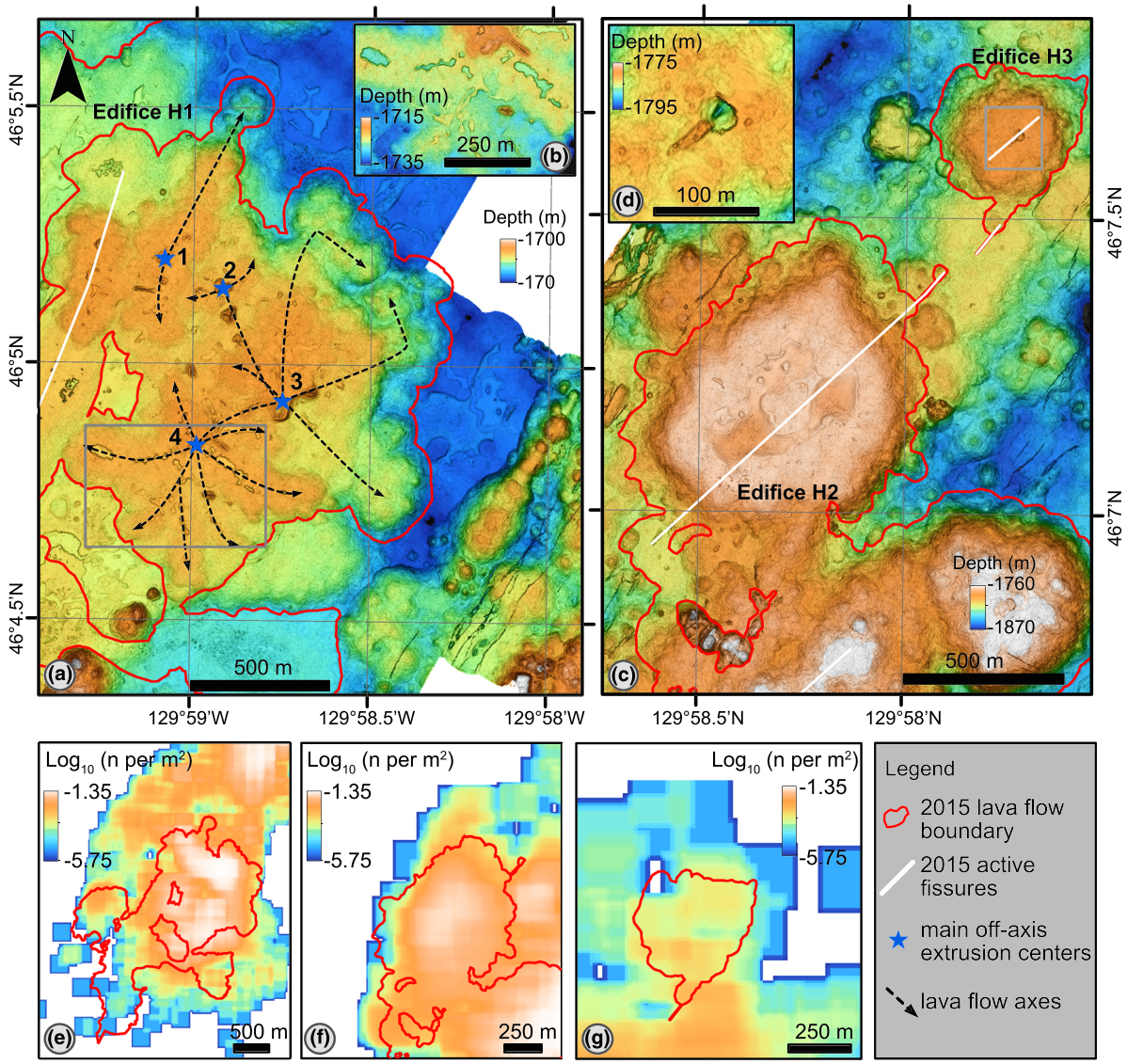

Figure 2. (a, c) Bathymetric map showing edifices H1 (a), H2, and H3 (c) outlined in red. White lines indicate eruptive fissures, and blue stars major off-axis extrusion centers on Edifice H1. The notation is similar in Figure 3 and Table 1. (b) Close-up of the complex structure of Edifice H1 located by a gray box in (a). (d) Close-up of the summit structure of edifice H3 located by a gray box in (c). (e–g) Map of the density of impulsive sounds in 25 × 25 m cell size represented by number of events per m^2, with a $\log_{10}$ color scale, shifted to fit the bathymetry (as documented in Figure S2). Edifices H1 (e), H2 (f), and H3 (g) are outlined in red.

continued along one axis while another burst started. From the extrusion centers, impulsive sounds migrated in all directions, in agreement with observations from the map data showing the distribution of the lobes emanating from each extrusion center. There is no clear relationship between the flow front velocity and the flow direction.

Similar spatial analyses of the distribution of impulsive sounds for Edifices H2 and H3 are shown in Figures 3c and 3d. Neither of those edifices is as complex as edifice H1, morphologically or acoustically. The activity at edifice H2 started about 11 hr after the beginning of the eruption and continued for about 113 hr (Table 1). Flow front propagation is only evident perpendicular to the fissure. The lava flows emanated simultaneously on the west and east flanks of the fissure (Figure 3c) at rates estimated to be 0.018 and 0.024 m s^{-1}, respectively (Table 1). During that period, most of the impulsive sounds occurred near the single extrusion center, where the growth of the edifice is associated with a second burst of impulsive events, while at the edges of the edifice, the number of impulsive sounds remained relatively constant

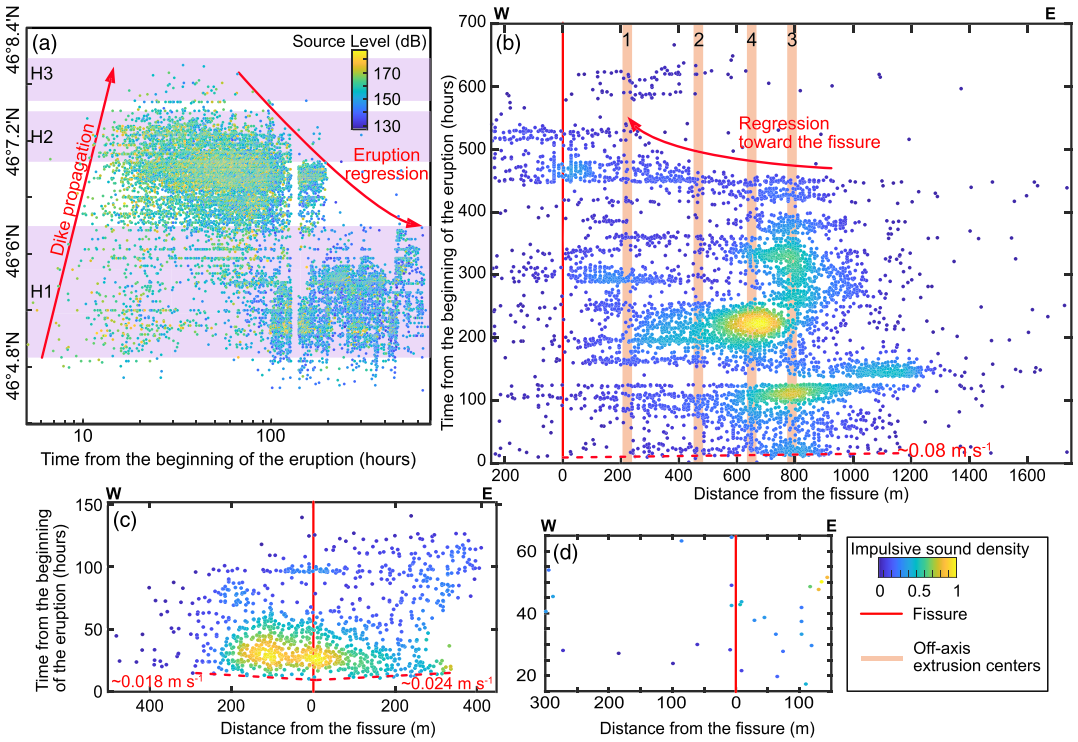

Figure 3. (a) Time distribution of the impulsive sounds as a function of latitude and colored depending on acoustic source level (dB re 1 μPa at 1 m). The location of the three edifices is indicated by a light purple background. Interpretations of dike propagation and flow regression as the eruption proceeded are shown by red arrows. (b–d) Time distribution of the impulsive sounds as a function of the distance from the fissure for edifice H1 (b), H2 (c), and H3 (d). Impulsive sound density is represented by the color code as a percent of the maximum density. The eruptive fissure is indicated by vertical red lines. Off-axis extrusion centers observed at edifice H1 are indicated by the bold orange lines numbered as in Figure 2a. On the profile Extrusion Center 4 appears closer to the fissure than Center 3, but analysis of the bathymetric data evidences the presence of a pressure ridge between the two extrusion centers suggests that Extrusion Center 4 was fed by a tube system passing under Extrusion Center 3. Initial flow propagation from H1 and H2 is indicated with red dashed lines. The impulsive sound time is represented in hours from the beginning of the acoustic activity at 8:01 UTC on 24 April. The average uncertainty in the location of the impulsive sounds is 140 m, with 68% confidence, plus a shift of 990 m toward the south for H1, and a shift of 540 and 123 m toward the east for H2 and H3 (Figure S2). Uncertainties on the flow velocity are reported in Table 1.

through the duration of hummock growth. Only a few impulsive sounds were recorded at Hummock H3. Their source is more difficult to define, so the values are uncertain (which is why they are not listed in Table 1), and no propagation rate can be estimated (Figure 3d).

4. Discussion

During the 2015 eruption, the flows emplaced on the north rift of Axial Seamount are thicker than those emplaced within or near the caldera (>60 m vs. <15 m, respectively; Chadwick et al., 2016). They are also characterized by more complex morphology, especially Edifice H1, where elongated collapses and extrusion sources, distant from the initial eruptive fissure, indicate the existence of an elaborate underlying tube system that connects the extrusion centers back to the eruptive fissure (Figure 2a; Clague et al., 2017; Yeo et al., 2013). Those hummocks are also the locations of higher impulsive sound densities and are associated with longer emplacement duration (Figures 3 and 4).

There is a direct relationship between the distribution of impulsive acoustic signals and the overall morphology of the edifices. Construction of H1 began with somewhat higher density sound signals as the surface flow emanated from the fissure and evolved with a succession of explosive bursts originating from multiple points within the flow (Figure 3b). The propagation length and direction of these bursts of acoustic signals coincide with the length and direction of individual channelized lobes identified on the AUV bathymetry (Figure 2a). At H2, the acoustic signals record distinct events that occurred during construction of the edifice such as the emplacement and inflation of sheet flows at its center. Furthermore, for H1 and H2, space-time patterns of

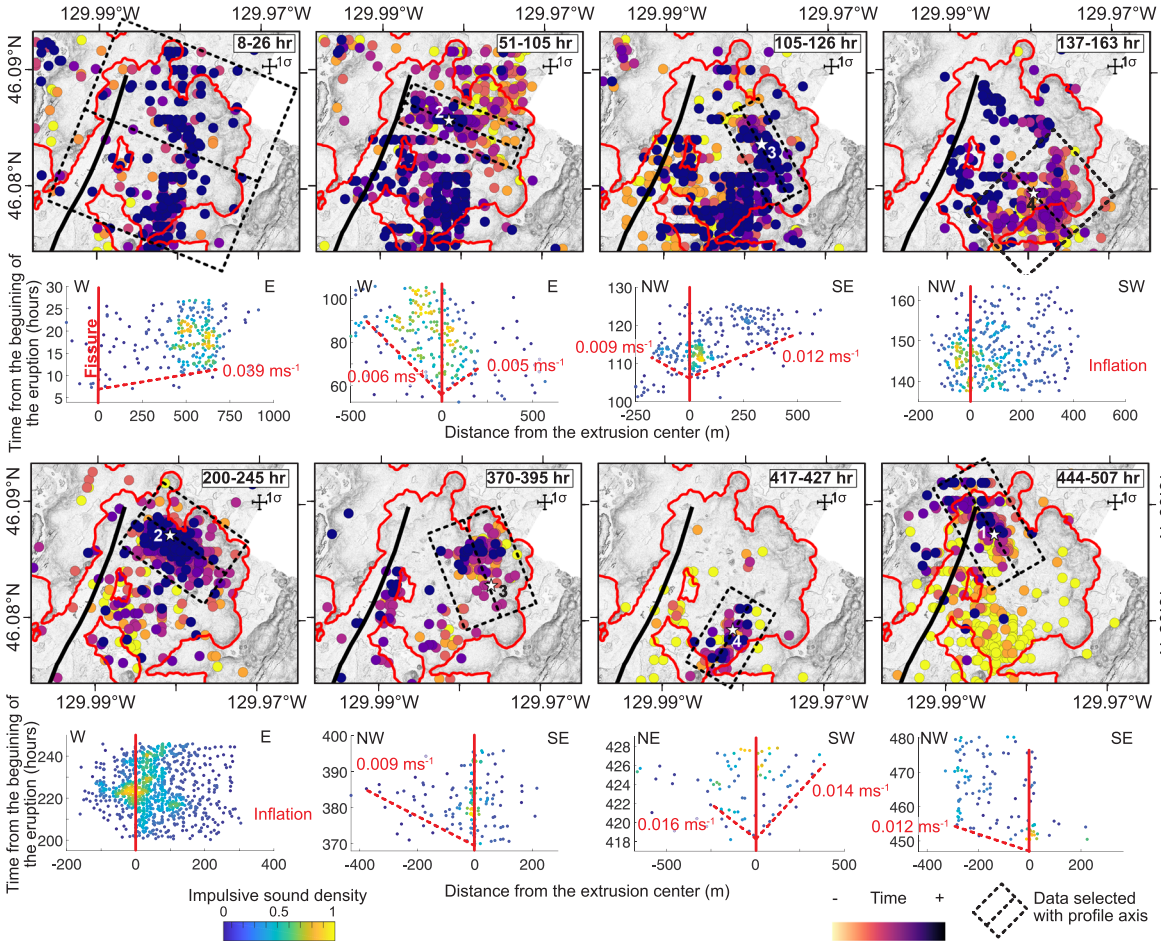

Figure 4. Illustration of the time-space evolution of the acoustic signal recorded at hummock H1 during the 2015 eruption. The eight maps show different periods of time during the eruption. The time period concerned is indicated in the upper left corner of each map in hours from the beginning of the acoustic activity at 8:01 UTC on 24 April. Flow boundaries determined from the bathymetric map are indicated in red and the eruptive fissure by a black line. Acoustic signals are represented by dots colored as a function of time from yellow to dark blue. The location uncertainty of the events estimated at ~140 m is represented by 1 σ on the map. The main extrusion centers are indicated by a white star as in Figure 2a. Plots of time versus distance from the extrusion center color by density of events similar to Figures 3b–3d. Each plot shows the propagation of the acoustic events along a profile during the corresponding time period of the map above it. Uncertainties on the flow velocity are reported Table 1. Extrusive centers are shown by vertical red lines, and flow front velocities are shown by the dashed projection lines. The bounds of the selected data and axes of the profiles are indicated on the maps by dashed frames.

acoustic signal bursts record how the flow lobes grew. Some acoustic signals bursts show a time-distance correlation (Figure 4) tracking the advance of the lava flow front away from the extrusion source. These bursts are associated with the emplacement of individual lobes of the hummocks over 8 to 100 hr. Other explosive bursts do not show a time-distance correlation and appear to occur along an entire lobe in areas where migrating bursts had occurred (Figures 3 and 4). The distribution and location along the axis of individual lobes indicate that these bursts are likely associated with the inflation of preexisting lobes (Table 1).

The origin of these impulsive acoustic signals has been the subject of discussion in the last decade. Two primary sources have been proposed. First, the acoustic signal could result from venting of magmatic gases (Chadwick et al., 2008; Schlindwein & Riedel, 2010; Tan et al., 2016). Direct observations of the NW Rota-1 volcano eruption in 2006 (Mariana Arc) (Chadwick et al., 2008) and the presence of pyroclastic deposits on the Gakkel ridge during the 1999–2001 volcanic activity (Schlindwein & Riedel, 2010; Sohn et al., 2008) indicate that the seismoacoustic bursts may result from the release of gas from slowly rising magma. The acoustic signal could also result from the interaction of lava with seawater (Caplan-Auerbach et al., 2017; Tan et al., 2016; Wilcock et al., 2016). Perfit et al. (2003) proposed that even at greater depth than at Axial,

Table 1
Duration, Length, and Flow-Front Velocity Extracted From Hydroacoustic Events for Edifices H1 and H2[a]

Burst initiation In hours from 08:01 UTC on the 4/24/2015[b]	Extrusion source[c]	Profile orientation (°N)	Flow direction	Lobe length (m)	Flow-front velocity[d] (m s^{-1})	Emplacement duration[e] (hr)
Edifice H1						
6.8	Fissure	110	E	629	0.039 ± 0.009	20.1
56.09	Ex2	109	E	184	0.006 ± 0.002	38.4
56.09	Ex2	109	W	473	0.004 ± 0.002	49.1
106.3	Ex3	144	SW	512	0.012 ± 0.003	19.6
106.3	Ex3	144	NE	173	0.009 ± 0.002	8.9
137.6	Ex4	139	inflation	469	—	25.9
201	Ex2	120	inflation	214	—	44.8
289	Ex1	137	inflation	300	—	13
289	Ex1	33	inflation	231	—	14
358	Ex2	137	inflation	314	—	5
370	Ex3	147	NE	430	0.009 ± 0.007	19.4
417	Ex4	44	SW	330	0.014 ± 0.007	18.6
417	Ex4	44	NE	250	0.016 ± 0.010	18.6
450	Ex1	145	W	183	0.013 ± 0.008	29.8
Edifice H2						
11.0	Fissure	127	NW	284.9	0.018	83
11.0	Fissure	127	SE	312.6	0.024	113
94	Fissure	127	inflation		—	5

[a]The method of calculation of flow propagation from the hydroacoustic data is described in Figure S3. [b]Hydroacoustic activity indicative of lava flows began on 24 April 2015 at 08:01 UTC (Wilcock et al., 2016). [c]The extrusion source names are referenced in Figure 2. [d]Uncertainties in velocity represent 68% confidence. [e]The emplacement duration is measured from the beginning of propagation from the extrusion center to the end of the acoustic activity along the entire lobe.

bubbles of vaporized sea water that rise through the base of the flow up to the upper-crust may contribute to the seismo-acoustic signals recorded during eruptions.

Although pyroclastic deposits have been found during the 2015 eruption of Axial Seamount, the distribution of ash observed on seafloor benchmarks within the caldera and the composition of the pyroclasts suggests that pyroclastic eruptions occurred only during the earliest stage of the eruption (Chadwick et al., 2016; Clague et al., 2018; Xu et al., 2018) whereas the acoustic signals are observed for the duration of the eruption. We propose that the impulsive acoustic signals recorded at Axial Seamount were steam explosions resulting from the infiltration of seawater under the crust of channelized flows, or into cracks during flow inflation. The highest density of the acoustic signals seems to have occurred during tumulus growth and reached a maximum for larger tumuli (e.g., Extrusion Center 4 at H1). The development of tumuli, associated with the formation of numerous cracks, support the hypothesis that impulsive signals were steam explosions, while low numbers of explosions after hummock growth indicates that they do not result from crust collapse after lava drains back into the fissure. The variations of the explosion pattern seem to be an indication of flow type, with these sounds being generated infrequently during the emplacement of mounds of pillow lavas (e.g., H3), more frequently in association with channelized flows, and at the highest density during inflation of hummocky flows.

Less is known about the longer-duration broadband signals that were also recorded between 1 and 20 May. Due to their diffuse character, they cannot be well located. Caplan-Auerbach et al. (2017) have proposed that they are the result of pyroclastic, ash-producing fire fountains. However, pyroclasts were only formed at the beginning of the 2015 eruption (Chadwick et al., 2016; Clague et al., 2018; Xu et al., 2018). Longer-duration broadband signals started to be recorded after the focus of eruptive activity began to regress back toward the caldera (Figure 3a) and continued until the end of the eruption. Therefore, an alternative hypothesis is that these prolonged diffuse signals are associated with the drainage of lava back into open fissures, as linear depressions with drainback features are evident within some of the flows (Chadwick et al., 2016; Clague et al., 2017).

The flow morphology of the hummocks, especially the large quantity of lava pillows preserved on the hummock surfaces, indicates that the eruption rate was already decreasing when the hummocks began to grow at

the distal end of the dike as it propagated northward. This is confirmed from the acoustic records, which suggest the dike propagation rate is ~0.3 m s^{-1} between 46°4.8′N and 46°7.8′N, about half the 0.7 m s^{-1} rate at which it propagated from the caldera to the north rift (Chadwick et al., 2016; Wilcock et al., 2016, 2018). A similar decrease of the dike propagation rate was observed in the 1998 eruption from seismic records (Dziak & Fox, 1999). Northward dike propagation ended 15 to 20 hr after the beginning of the eruption and was rapidly followed by the regression of eruptive activity back toward the caldera while Edifices H1, H2, and H3 were still being constructed (Figure 3a). These changes of dike pressure and extrusion rate are consistent with the evolution of extrusion rate and flow-front advancement measured at H1 and H2. While the dike was propagating, flow-front velocities are estimated to have been 0.018 to 0.039 m s^{-1}, whereas they dropped mostly below 0.016 m s^{-1} during the regression of the eruption (Figure 3a; Table 1). These rates are significantly higher than what would have been inferred as a time-averaged advance rate. Indeed, only brief periods of the eruption are associated with flow advancement, and most of the volume erupted contribute to the vertical growth of those mounds via inflation. However, these flow advancement rates are slower than were measured for channelized flows emplace during 2005–2006 eruption of the EPR and 2011 eruption of Axial Seamount and determined using similar methods (0.03 to 0.31 m s^{-1}; Tan et al., 2016) or numerical modeling of diffusion-controlled bubble growth (0.02 to 0.7 m s^{-1}; Jones et al., 2018; Soule et al., 2012). Similar to the advancement rates, the average extrusion rates estimated for the three inflated hummocks of 22 to 53 m^3 s^{-1} is also slightly lower than the 100 m^3 s^{-1} estimates for the 2005–2006 eruption on the EPR (Tan et al., 2016). However, this is consistent with the difference of lava flow morphology: sheet flows to lobate flows for the EPR and lobate flows to pillow flows for the hummocks. The extrusion rates for the hummocky mounds fall in the range of extrusion rates estimated from the duration of seismic swarms elsewhere along the Juan de Fuca ridge and at Axial Seamount. It is 1 order of magnitude higher than the one estimated for the production of pillow mounds (3.5 to 5.5 m^3 s^{-1}; Yeo et al., 2013), and 1 to 2 orders of magnitude lower than extrusion rates estimated for channelized flows (500 to 2,400 m^3 s^{-1}; Chadwick et al., 2013).

The regression of the eruptive activity back toward the caldera appears to stall at Edifice H1 (Figure 3a). However, the cessation of the eruption is seen in the summit morphology of H1. The collapses in the upper parts of the lobes (Figure 2c) are consistent with a progressive decrease in the pressure in the underlying tube system as supply decreased and lava drained toward the end of the eruption (e.g., Chadwick et al., 2013), and the eruptive activity migrated from the off-axis extrusion centers toward the fissure (Figure 3b). When the pressure became insufficient to transport lava further off-axis against a thickening lava crust, ephemeral pulses of lava heaved up the tumuli over the extrusion centers on H1 and H3 (Figures 2a and 2g) and overflowed at the summit of H2 to build the levees (Figure 2d). These complex hummocks observed on the north rift are not unique at Axial Seamount, as prehistoric examples are present on the north and south rifts as illustrated, but not described, in Clague et al. (2013, 2017). Their morphological similarity and their distal location from the caldera could indicate that this type of edifice is constructed during long-duration eruptions near the end of a propagating dike.

5. Conclusions

The dynamics of the 2015 eruption along the north rift of Axial Seamount are elucidated by combining detailed seafloor bathymetry of the newly formed flows with a record of the impulsive acoustic sounds generated by the interaction of lava and seawater. Hummocky mounds were constructed ~9.5 to 15.5 km down rift from the caldera over time scales of 2 to 28 days. The northern-most mounds were formed over the first few days of the eruption, after which eruptive activity regressed back toward the caldera, where a larger and more complex mound with multiple eruptive centers was formed over the next 3 weeks. There is no evidence that the volume erupted was correlated with the number of acoustic events recorded. Instead, the amount of acoustic activity seems better correlated with the dynamics of the eruption. Low eruption-rate flows forming pillow lavas appear to have produced fewer sounds; therefore, these signals may provide only a minimum duration of flow emplacement. Sounds were produced more commonly during the emplacement of surface channelized flows, and the highest density of signals was produced during flow inflation and expansion. The time-space pattern of the impulsive sounds shows that hummocks may result from the alternation between the emplacement of a new lobe and the inflation of preexisting lobes.

Data Availability Statement

The AUV bathymetric maps and flow contours are available through the IEDA database (https://doi.org/10.26022/IEDA/329694 and 10.1594/IEDA/324417, respectively). Raw OOI seismic and hydrophone data are available through the IRIS Data Management Center (http://ds.iris.edu/gmap/#network=OO&planet=earth/). The impulsive event catalog is available through the IEDA database (https://doi.org/10.26022/IEDA/329763).

Acknowledgments

This work was possible due to repeated ship-based and AUV bathymetric surveys and the OOI cabled array at Axial Seamount. Special thanks go to the crews of MBARI's ships R/V *Rachel Carson* and R/V *Western Flyer* and the MBARI ROV and AUV operations teams as well as to the crews of R/V *Thomas Thompson* and R/V *Atlantis*. We also thank I. Yeo and the two anonymous reviewers for their constructive comments that have helped to improve this manuscript. Analysis of the hydroacoustic signals was supported by NSF OCE-1635276. This work was conducted during a postdoctoral fellowship at MBARI funded by the David and Lucile Packard Foundation.

References

Caplan-Auerbach, J., Dziak, R. P., Haxel, J., Bohnenstiehl, D. R., & Garcia, C. (2017). Explosive processes during the 2015 eruption of Axial Seamount, as recorded by seafloor hydrophones. *Geochemistry, Geophysics, Geosystems*, *18*, 1761–1774. https://doi.org/10.1002/2016GC006734

Caress, D. W., Clague, D. A., Paduan, J. B., Martin, J., Dreyer, B., Chadwick, W. W. Jr., et al. (2012). Repeat bathymetric surveys at 1-metre resolution of lava flows erupted at Axial Seamount in April 2011. *Nature Geoscience*, *5*(7), 483–488. https://doi.org/10.1038/NGEO1496

Chadwick, W. W., Cashman, K. V., Embley, R. W., Matsumoto, H., Dziak, R. P., de Ronde, C. E. J., et al. (2008). Direct video and hydrophone observations of submarine explosive eruptions at NW Rota-1 volcano, Mariana arc. *Journal of Geophysical Research*, *113*, B08S10. https://doi.org/10.1029/2007JB005215

Chadwick, W. W., Clague, D. A., Embley, R. W., Perfit, M. R., Butterfield, D. A., Caress, D. W., et al. (2013). The 1998 eruption of Axial Seamount: New insights on submarine lava flow emplacement from high-resolution mapping. *Geochemistry, Geophysics, Geosystems*, *14*, 3939–3968. https://doi.org/10.1002/ggge.20202

Chadwick, W. W., Paduan, J. B., Clague, D. A., Dreyer, B. M., Merle, S. G., Bobbitt, A. M., et al. (2016). Voluminous eruption from a zoned magma body after an increase in supply rate at Axial Seamount. *Geophysical Research Letters*, *43*, 12,063–12,070. https://doi.org/10.1002/2016GL071327

Clague, D. A., Dreyer, B. M., Paduan, J. B., Martin, J. F., Chadwick, W. W., Caress, D. W., et al. (2013). Geologic history of the summit of Axial Seamount, Juan de Fuca Ridge. *Geochemistry, Geophysics, Geosystems*, *14*, 4403–4443. https://doi.org/10.1002/ggge.20240

Clague, D. A., Paduan, J. B., Caress, D. W., Chadwick, W. W. Jr., le Saout, M., Dreyer, B. M., & Portner, R. A. (2017). High-resolution AUV mapping and targeted ROV observations of three historical lava flows at Axial Seamount. *Oceanography*, *30*(4). https://doi.org/10.5670/oceano.2017.426

Clague, D. A., Paduan, J. B., Dreyer, B. M., Chadwick, W. W. Jr., Rubin, K. R., Perfit, M. R., & Fundis, A. T. (2018). Chemical variations in the 1998, 2011, and 2015 lava flows from Axial Seamount, Juan de Fuca Ridge: Cooling during ascent, lateral transport, and flow. *Geochemistry, Geophysics, Geosystems*, *19*, 2915–2933. https://doi.org/10.1029/2018GC007708

Dziak, R. P., & Fox, C. G. (1999). The January 1998 earthquake swarm at Axial Volcano, Juan de Fuca Ridge: Hydroacoustic evidence of seafloor volcanic activity. *Geophysical Research Letters*, *26*(23), 3429–3432. https://doi.org/10.1029/1999GL002332

Gregg, T. K. P., & Fink, J. H. (1995). Quantification of submarine lava-flow morphology through analog experiments. *Geology*, *23*(1), 73–76. https://doi.org/10.1130/0091-7613(1995)023<0073:QOSLFM>2.3.CO;2

Griffiths, R. W., & Fink, J. H. (1992). Solidification and morphology of submarine lavas: A dependence on extrusion rate. *Journal of Geophysical Research*, *97*(B13), 19,729–19,737. https://doi.org/10.1029/92JB01594

Jones, M. R., Soule, S. A., Gonnermann, H. M., le Roux, V., & Clague, D. A. (2018). Magma ascent and lava flow emplacement rates during the 2011 Axial Seamount eruption based on CO_2 degassing. *Earth and Planetary Science Letters*, *494*, 32–41. https://doi.org/10.1016/j.epsl.2018.04.044

Kelley, D. S., Delaney, J. R., & Juniper, S. K. (2014). Establishing a new era of submarine volcanic observatories: Cabling Axial Seamount and the Endeavour Segment of the Juan de Fuca Ridge. *Marine Geology*, *352*, 426–450. https://doi.org/10.1016/j.margeo.2014.03.010

Mann, M. E., Bohnenstiehl, D. R. & Weis, J. (2016). Waveform template matching and analysis of hydroacoustic events from the April–May 2015 eruption of Axial Volcano. Abstract OS41C-1993 Presented at Fall Meeting, American Geophysical Union, San Francisco, CA.

Meyer, J. D., & White, S. M. (2007). Lava morphology mapping by expert system classification of high-resolution side-scan sonar imagery from the East Pacific Rise, 9°–10°N. *Marine Geophysical Researches*, *28*(2), 81–93. https://doi.org/10.1007/s11001-007-9015-8

Nooner, S. L., & Chadwick, W. W. (2016). Inflation-predictable behavior and co-eruption deformation at Axial Seamount. *Science*, *354*(6318), 1399–1403. https://doi.org/10.1126/science.aah4666

Perfit, M., Cann, J., Fornari, D. J., Engels, J., Smith, D. K., Ridley, W. I., & Edwards, M. H. (2003). Interaction of sea water and lava during submarine eruptions at mid-ocean ridges. *Nature*, *426*(6962), 62–65. https://doi.org/10.1038/nature02032

Schlindwein, V., Müller, C., & Jokat, W. (2005). Seismoacoustic evidence for volcanic activity on the ultraslow-spreading Gakkel ridge, Arctic Ocean. *Geophysical Research Letters*, *32*, L18306. https://doi.org/10.1029/2005GL023767

Schlindwein, V., & Riedel, C. (2010). Location and source mechanism of sound signals at Gakkel Ridge, Arctic Ocean: Submarine Strombolian activity in the 1999-2001 volcanic episode. *Geochemistry, Geophysics, Geosystems*, *11*, Q01002. https://doi.org/10.1029/2009GC002706

Sohn, R., Willis, C., Humphris, S., Shank, T. M., Singh, H., Edmonds, H. N., et al. (2008). Explosive volcanism on the ultraslow-spreading Gakkel ridge, Arctic Ocean. *Nature*, *453*(7199), 1236–1238. https://doi.org/10.1038/nature07075

Soule, S. A., Fornari, D. J., Perfit, M. R., & Rubin, K. H. (2007). New insights into mid-ocean ridge volcanic processes from the 2005–2006 eruption of the East Pacific Rise, 9°46′N–9°56′N. *Geology*, *35*(12), 1079–1082. https://doi.org/10.1130/G23924A.1

Soule, S. A., Nakata, D. S., Fornari, D. J., Fundis, A. T., Perfit, M. R., & Kurz, M. D. (2012). CO2 variability in mid-ocean ridge basalts from syn-emplacement degassing: Constraints on eruption dynamics. *Earth and Planetary Science Letters*, *327–328*, 39–49.

Tan, Y. J., Tolstoy, M., Waldhauser, F., & Wilcock, W. S. (2016). Dynamics of a seafloor-spreading episode at the East Pacific Rise. *Nature*, *540*(7632), 261–265. https://doi.org/10.1038/nature20116

Tolstoy, M., Cowen, J. P., Baker, E. T., Fornari, D. J., Rubin, K. H., Shank, T. M., et al. (2006). A sea-floor spreading event captured by seismometers. *Science*, *314*(5807), 1920–1922. https://doi.org/10.1126/science.1133950

Wilcock, W. S., Dziak, R. P., Tolstoy, M., Chadwick, W. W. Jr., Nooner, S. L., Bohnenstiehl, D. R., et al. (2018). The recent volcanic history of Axial Seamount: Geophysical insights into past eruption dynamics with an eye toward enhanced observations of future eruptions. *Oceanography*, *31*(1), 114–123. https://doi.org/10.5670/oceanog.2018.117

Wilcock, W. S., Tolstoy, M., Waldhauser, F., Garcia, C., Tan, Y. J., Bohnenstiehl, D. R., et al. (2016). Seismic constraints on caldera dynamics from the 2015 Axial Seamount eruption. *Science*, *354*(6318), 1395–1399. https://doi.org/10.1126/science.aah5563

Xu, G., Chadwick, W. W. Jr., Wilcock, W. S., Bemis, K. G., & Delaney, J. (2018). Observation and modeling of hydrothermal response to the 2015 eruption at Axial Seamount, Northeast Pacific. *Geochemistry, Geophysics, Geosystems*, *19*, 2780–2797. https://doi.org/10.1029/2018GC007607

Yeo, I. A., Clague, D. A., Martin, J. F., Paduan, J. B., & Caress, D. W. (2013). Preeruptive flow focussing in dikes feeding historical pillow ridges on the Juan de Fuca and Gorda Ridges. *Geochemistry, Geophysics, Geosystems*, *14*, 3586–3599. https://doi.org/10.1002/ggge.20210